Power Electronics Research and Applications Transactions
https://www.sciltp.com/journals/perat

Article

A Load-Adaptive Virtual Resistance Strategy for Decentralized Control of Low-Voltage Islanded Microgrids

Ashitha Pallen *, Jiefeng Hu and Syed Islam

Centre for New Energy Transition Research, Federation University, Mount Helen, VIC 3353, Australia
* Correspondence: apallen@students.federation.edu.au

How To Cite: Pallen, A.; Hu, J.; Islam, S. A Load-Adaptive Virtual Resistance Strategy for Decentralized Control of Low-Voltage Islanded Microgrids. *Power Electronics Research and Applications Transactions* **2026**. https://doi.org/10.53941/perat.2026.100008

Received: 29 July 2026
Revised: 14 September 2026
Accepted: 17 September 2026
Published: 23 September 2026

Abstract: The voltage regulation of inverter-based islanded microgrids with virtual impedance frequently deteriorates under higher load demand due to voltage drops across the virtual impedance and the feeder. Conventional droop control with a fixed virtual resistance (R_v) improves current sharing by impedance matching but amplifies voltage sag as the load increases. This paper proposes a novel load-adaptive virtual resistance strategy for decentralized control of low-voltage microgrids. Unlike conventional fixed virtual resistance methods and many existing adaptive virtual impedance approaches, the proposed method directly embeds a prescribed voltage-regulation coefficient into the R_v formulation. The adaptive virtual resistance is analytically determined using the allowable voltage deviation, inverter rating, feeder resistance, and locally measured dq-axis voltage and current components. As the load demand increases, the calculated virtual resistance decreases automatically, thereby limiting the voltage drop introduced by the virtual resistance while preserving proportional power sharing among parallel inverters. The adaptive law is implemented in the dq reference frame using locally measured voltages and currents. A cascaded PI controller structure comprising an inner current loop and an outer voltage loop is used for control. Comprehensive tests under various load change scenarios are conducted to evaluate the proposed approach, and the results demonstrate improved voltage regulation under wide load variations. Moreover, the proposed approach improves reactive power sharing, which is a significant challenge in inverter-based microgrids. The proposed method is simple, fully decentralized, and can be integrated into existing droop-controlled inverters without communication links.

Keywords: adaptive virtual resistance; droop control; islanded operation; low-voltage microgrid; reactive power; voltage regulation

1. Introduction

The low-voltage (LV) microgrids are a promising solution for integrating various distributed generation (DG) units, such as PV inverters, battery energy storage systems (BESS), and small wind turbines, into local power networks [1,2]. As the generation is closer to the load, LV microgrids can reduce transmission losses, improve energy efficiency, and enhance modularity and flexibility, making them a viable solution for residential communities and remote areas. Islanded microgrids offer better supply reliability, more efficient use of renewable sources, and improved resilience during grid disturbances compared to traditional radial distribution systems [3]. However, in the absence of a grid, inverters must regulate voltage and frequency autonomously, posing significant challenges for the development of robust control strategies, as a poorly designed control approach can lead to deviations in voltage and frequency [4–6]. The general structure of a low-voltage islanded microgrid with multiple DG units connected to the point of common coupling (PCC) is shown in Figure 1.

Droop control is widely adopted for decentralized power sharing among parallel inverters, as it can mimic the behavior of synchronous generators, avoiding the need for communication links [4,7–10]. Classical droop control performs well in medium and high voltage systems where Feeder impedances are predominantly inductive [11].

However, the voltage regulation and power-sharing accuracy deteriorate in LV microgrids due to the resistive nature of feeder impedance and the resulting coupling between active and reactive powers [6,12–14]. The droop concept originates from the steady-state characteristics of synchronous generators, in which the frequency and voltage magnitude drops with increasing active power and reactive power respectively.

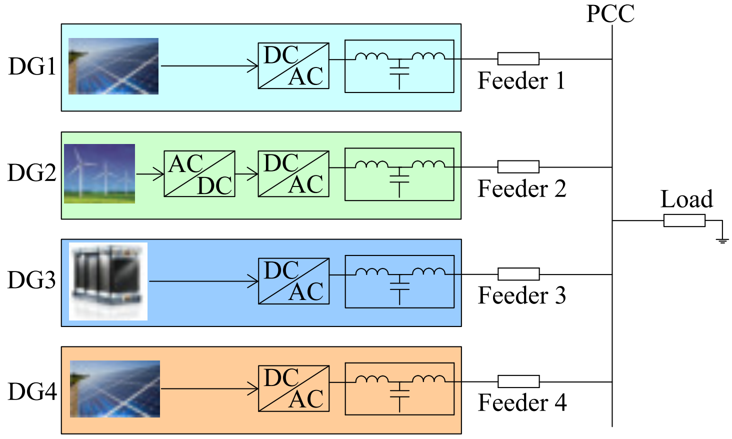

Figure 1. Structure of the low-voltage islanded microgrid with multiple DG units.

A microgrid with multiple inverters, the frequency and a voltage reference for each unit can be generated by conventional droop control as follows:

$$\omega_i^* = \omega - n_{p,i} P_i \tag{1}$$
$$V_i^* = V - m_{q,i} Q_i \tag{2}$$

where ω_i^* and V_i^* are the frequency and voltage magnitude references generated by the i^{th} inverter, respectively. ω and V are the nominal system frequency and voltage, respectively. $P_i$and Q_i are the real and reactive powers, respectively, measured at the output of each DG unit. Frequency and voltage droop coefficients are denoted by $n_{p,i}$ and $m_{q,i}$, respectively.

The above droop control law is primarily applicable to systems with inductive line impedance, where active power predominantly influences frequency and reactive power affects voltage magnitude. However, in LV microgrids, the line impedance is mainly resistive, resulting in a coupling between the active and reactive powers. Consequently, the conventional droop law becomes ineffective, and the droop characteristics are reversed, leading to the inverse droop control strategy [8,13–15], which can be expressed as:

$$\omega_i^* = \omega + n_{q,i} Q_i \tag{3}$$
$$V_i^* = V + m_{p,i} P_i \tag{4}$$

where $n_{q,i}$, $m_{p,i}$ represent the newly defined droop coefficients associated with the reactive power and active power, respectively.

Although the inverse droop law effectively accounts for the resistive nature of low-voltage microgrids, the trade-off between accurate power sharing and voltage regulation remains inevitable. Moreover, the power sharing inaccuracy caused by line impedance mismatches is not addressed in this approach.To overcome this power sharing limitation, a virtual resistance (R_v) is introduced to compensate for the impedance differences among distributed generation (DG) units, thereby achieving more accurate power sharing. However, the inclusion of virtual resistance alters the voltage reference at the inverter output as an additional voltage drop is introduced in series with the line impedance as in Figure 2, and the voltage reference now becomes:

$$\begin{aligned} V_{ref,i} &= V_i^* - (R_{line,i} + R_{v,i}) I_{o,i} \\ &= V_i^* - R_{eq,i} I_{o,i} \end{aligned} \tag{5}$$

Here $R_{line,i}$ refers to the actual feeder resistance, $R_{v,i}$ is the virtually inserted resistance used for impedance reshaping, $R_{eq,i} = R_{line,i} + R_{v,i}$ denotes the total equivalent resistance, and $I_{o,i}$ denotes the corresponding inverter output current at the PCC.

https://doi.org/10.53941/perat.2026.100008

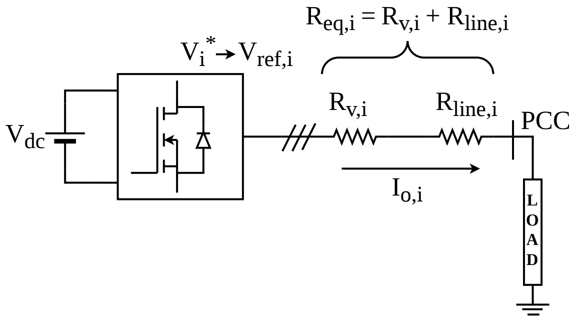

Figure 2. Equivalent circuit of inverter i showing the virtual resistance and line resistance in a low-voltage microgrid.

The total voltage drop across each feeder, arising from both the physical line resistance and the virtually inserted resistance, can be approximated as:

$$\triangle V_i = R_{eq,i} I_{o,i} \tag{6}$$

Even with inverse droop, unequal feeder resistances and mismatched inverter ratings lead to power sharing errors and voltage imbalance. Virtual impedance control especially virtual resistance has therefore been widely introduced to reshape the effective output impedance and equalize power sharing without communication [6,16–20]. However, a fixed virtual resistance creates a trade-off where higher values improve power sharing but increase voltage drop, while lower values preserve voltage regulation but reduce sharing accuracy. As a result, fixed virtual-impedance designs often struggle to maintain acceptable voltage regulation in low-voltage systems.

To overcome this limitation, several adaptive virtual resistance (AVR) methods have been proposed, where the virtual impedance is adjusted online based on current, voltage deviation, or power sharing error [5,21–28]. These methods improve performance under varying load conditions but commonly lack an explicit mechanism to enforce a guaranteed voltage regulation boundary. Additionally, some rely on communication links or exchange of control signals, which increase system complexity and vulnerability. In [29], adaptive virtual impedance regulation is employed to improve fundamental and harmonic power sharing accuracy in islanded multibus microgrids, with secondary control used for frequency and average voltage recovery. Nevertheless, the approach prioritizes power sharing performance, resulting in noticeable voltage deviations at the inverter buses under varying load conditions. Accurate power sharing with voltage regulation is achieved in [30–32]. however, the reliance on communication links makes these approaches more complex and less robust.

Recent studies have also investigated optimized droop and virtual-impedance design to improve the stability, power quality, and sharing performance of inverter-dominated microgrids [5–7,10,20,33]. Universal droop control and self-synchronized droop control have been introduced to improve the applicability of inverter control under different output impedance conditions [8, 9]. Although these methods improve the generality and dynamic performance of droop-controlled inverters, they mainly focus on controller optimization, impedance shaping, or power-sharing improvement. Therefore, the direct relationship between the selected virtual resistance and the allowable voltage drop is not explicitly embedded in the control law.

Motivated by these challenges, this paper proposes a load adaptive virtual resistance strategy for decentralized inverter control in low-voltage islanded microgrids. The key idea is to analytically determine the virtual resistance, required to maintain the inverter bus voltage within the limit and realize it through a dq frame virtual resistance law using local voltage and current measurements. A regulation coefficient is introduced which defines the maximum allowable voltage drop, and the resulting adaptive resistance is formulated as an explicit function of inverter rating and measured PCC voltage and current.

The main contributions of this paper are summarized as follows:

- A load-adaptive virtual resistance formulation is developed for low-voltage islanded microgrids by explicitly relating the virtual resistance to the allowable voltage deviation.
- The proposed method is implemented in the synchronous dq reference frame using locally measured voltage and current components, avoiding communication links among inverter units.
- The adaptive resistance is designed to decrease under heavier loading conditions, thereby reducing the excessive voltage drop caused by fixed virtual resistance while maintaining proportional power sharing among parallel inverters.

- The effectiveness of the proposed strategy is evaluated under different loading conditions and compared with the conventional fixed virtual resistance approach.

Table 1 highlights the key distinction of the proposed method compared with fixed virtual resistance and existing adaptive virtual impedance approaches. The proposed strategy does not require communication and directly relates the adaptive R_v to the selected voltage-regulation boundary, which is usually not explicitly considered in existing methods.

Table 1. Comparison of different virtual-resistance and adaptive impedance control approaches.

Method	Communication	Voltage Regulation Boundary	Virtual Resistance Linked to Allowable Voltage Drop	Power-Sharing Performance
Conventional fixed virtual resistance	No	No	No	Improved sharing, but voltage sag increases under heavy load
Existing adaptive virtual impedance/resistance methods	may be required	Usually not explicit	not directly included	Improved sharing, but voltage regulation may depend on tuning or secondary control
Proposed load-adaptive virtual resistance method	No	Yes	Yes	Proportional sharing with improved voltage regulation

The remainder of this paper is organized as follows. Section 2 describes the proposed load-adaptive virtual-resistance controller and its dq-domain formulation. Section 3 presents the simulation results and performance analysis under various loading conditions, followed by the conclusion in Section 4.

2. Proposed Control Strategy of Load Adaptive Virtual Resistance Based Droop Control

The proposed control strategy aims to enhance voltage regulation and power-sharing accuracy in islanded low-voltage microgrids by adaptively tuning the virtual resistance in real time. Instead of maintaining a constant R_v, the controller dynamically modifies the virtual resistance according to the load condition and the voltage deviation across each inverter terminal. This adaptive adjustment reduces the excessive voltage drop caused by fixed virtual resistance under heavy loading conditions while preserving proportional load sharing among parallel inverters.

2.1. Determination of Load Adaptive Virtual Resistance

For a three-phase islanded microgrid with predominantly resistive feeder impedance, the inverter output current component aligned with the PCC voltage can be approximated as

$$I_{o,i} \approx \frac{P_{load,i}}{3V_{bus,i}} \tag{7}$$

where $P_{load,i}$ denotes the active power delivered by the i^{th} inverter and $V_{bus,i}$ represents the RMS voltage measured at the PCC of the corresponding inverter.

Using this expression, the voltage drop across the equivalent resistive path can be written as

$$\Delta V_i = R_{eq,i} \frac{P_{load,i}}{3V_{bus,i}} \tag{8}$$

To explicitly define the voltage regulation behavior, a voltage regulation coefficient ϵ is introduced as

$$\epsilon = \frac{\Delta V_i}{V_{bus,i}}. \tag{9}$$

The parameter ϵ represents the allowable voltage deviation with respect to the inverter bus voltage. By selecting ϵ according to the desired voltage regulation limit, the virtual resistance can be adjusted in relation to the permitted voltage drop.

Dividing the voltage-drop expression by $V_{bus,i}$, we obtain

$$\epsilon = \frac{R_{eq,i} P_{load,i}}{3V_{bus,i}^2}. \tag{10}$$

By rearranging, the required equivalent resistance of the i^{th} inverter is obtained as

$$R_{eq,i} = \frac{3\epsilon V_{bus,i}^2}{P_{load,i}}. \tag{11}$$

To achieve proportional load sharing, the load power of each inverter is distributed according to its apparent power rating:

$$P_{load,i} = P_{total}\frac{S_i}{\sum_{j=1}^{N} S_j} \tag{12}$$

where P_{total} represents the total active power demand of the microgrid, S_i denotes the apparent power rating of the i^{th} inverter, and $\sum_{j=1}^{N} S_j$ indicates the combined apparent power rating of all parallel inverters.

The equivalent resistance consists of the feeder resistance and the virtual resistance:

$$R_{eq,i} = R_{line,i}^{est} + R_{v,i} \tag{13}$$

where $R_{line,i}^{est}$ is the estimated feeder resistance used in the controller. Substituting the rating-based power-sharing expression into the equivalent resistance equation gives the calculated virtual resistance as

$$R_{v,i}^{cal} = \frac{3\epsilon \sum_{j=1}^{N} S_j}{S_i}\frac{V_{bus,i}^2}{P_{total}} - R_{line,i}^{est}. \tag{14}$$

The feeder resistance can be obtained from cable parameters during installation or from an offline voltage-drop test during commissioning. From cable data, it can be approximated as

$$R_{line,i}^{est} = r_{cable} l_i \left[1 + \alpha_T (T_i - T_0)\right] \tag{15}$$

where r_{cable} is the conductor resistance per unit length at the reference temperature T_0, l_i is the feeder length, α_T is the temperature coefficient of the conductor, and T_i is the estimated operating temperature.

Alternatively, during commissioning, the feeder resistance can be estimated from the measured feeder voltage drop and current as

$$R_{line,i}^{est} = \frac{\Delta V_{line,i}}{I_{o,i}} \tag{16}$$

where $\Delta V_{line,i}$ is the measured voltage drop along the feeder and $I_{o,i}$ is the corresponding output current.

The virtual resistance is transformed into the synchronous rotating dq reference frame to simplify implementation and allow direct use of measured voltage and current components. In the abc frame, inverter voltages and currents vary sinusoidally with time, whereas in the dq frame they appear as controlled quantities under balanced operation.

The voltage magnitude in the dq frame is expressed as

$$V_{bus,i}^2 = \left(\frac{V_{d,i}}{\sqrt{2}}\right)^2 + \left(\frac{V_{q,i}}{\sqrt{2}}\right)^2 \tag{17}$$

and the active power is calculated as

$$P_i = \frac{3}{2}\left(V_{d,i} I_{d,i} + V_{q,i} I_{q,i}\right). \tag{18}$$

Using the proportional power-sharing relation in (12), the total active power is locally estimated from the measured output power of the i^{th} inverter as

$$P_{total,i}^{est} = P_i \frac{\sum_{j=1}^{N} S_j}{S_i}.$$

Accordingly, the calculated virtual resistance in the dq frame becomes

$$R_{v,i}^{cal} = \frac{3\epsilon \sum_{j=1}^{N} S_j}{2S_i}\frac{V_{d,i}^2 + V_{q,i}^2}{P_{total,i}^{est} + P_{\min}} - R_{line,i}^{est} \tag{19}$$

or

$$R_{v,i}^{cal} = K_i \frac{V_{d,i}^2 + V_{q,i}^2}{P_{total,i}^{est} + P_{\min}} - R_{line,i}^{est} \tag{20}$$

where

$$K_i = \frac{3\epsilon \sum_{j=1}^{N} S_j}{2S_i}. \tag{21}$$

Here, $V_{d,i}$ and $V_{q,i}$ denote the d- and q-axis voltage components of the i^{th} inverter, while $I_{d,i}$ and $I_{q,i}$ represent the corresponding current components in the synchronous rotating reference frame. The small positive term $P_{\min}$ is introduced to avoid division by a very small power value during startup and light-load operation.

Since $P_{total,i}^{est}$ is determined from the locally measured inverter active power and the known inverter ratings, the adaptive virtual-resistance calculation does not require communication of active-power measurements between the parallel units.

For practical implementation, the calculated virtual resistance is constrained within predefined limits:

$$R_{v,i}^{*} = \text{sat}\left(R_{v,i}^{cal}, R_{v,\min}, R_{v,\max}\right) \tag{22}$$

where $R_{v,\min}$ and $R_{v,\max}$ are the minimum and maximum allowable virtual resistance values, respectively. This limitation prevents negative or excessively large resistance values during transient or low-load conditions.

The applied virtual resistance is then updated smoothly as

$$R_{v,i}[k] = R_{v,i}[k-1] + \alpha_R \left(R_{v,i}^{*}[k] - R_{v,i}[k-1]\right) \tag{23}$$

where $0 < \alpha_R \leq 1$ determines the adaptation speed. In addition, the rate of change is limited by

$$|R_{v,i}[k] - R_{v,i}[k-1]| \leq \Delta R_{v,\max}. \tag{24}$$

These constraints prevent abrupt variation of the virtual resistance and reduce possible interaction with the inner voltage and current control loops. The adaptation factor α_R is selected such that the adaptive virtual-resistance dynamics remain slower than the inner voltage and current control dynamics, thereby limiting dynamic interaction between the adaptive and inner control loops.

Finally, the adaptive virtual resistance is introduced into the voltage reference generation as

$$V_{d,ref,i} = V_{d,i}^{*} - R_{v,i} I_{d,i} \tag{25}$$

$$V_{q,ref,i} = V_{q,i}^{*} - R_{v,i} I_{q,i} \tag{26}$$

where $V_{d,i}^{*}$ and $V_{q,i}^{*}$ are the voltage references generated by the inverse droop controller. Thus, the adaptive virtual resistance modifies the voltage reference according to the loading condition and the selected voltage regulation coefficient. As the load increases, the calculated R_v decreases, thereby limiting the voltage drop introduced by the virtual resistance and improving PCC voltage regulation compared with the fixed R_v method.

2.2. Detailed Control Structure of the Proposed Adaptive R_v Method

To implement the proposed load-adaptive virtual resistance strategy, a multi-loop hierarchical control structure is used, as shown in Figure 3. The proposed controller combines instantaneous power estimation, inverse droop control, adaptive virtual resistance generation, voltage-reference correction, an outer voltage regulation loop, and an inner current control loop.

The main purpose of this structure is to reduce the excessive voltage sag caused by the combined effect of feeder resistance and fixed virtual resistance, especially during high-load operation. Instead of using a constant virtual resistance, the proposed method calculates the virtual resistance according to the operating condition. Therefore, the effective output resistance of each inverter is adjusted dynamically based on the local load demand.

The controller is implemented independently for each inverter unit using only local voltage and current measurements. The measured three-phase voltages and currents are transformed from the abc frame to the synchronous rotating dq frame. In the dq frame, the active power P_i is calculated according to (18), while the reactive power of the i^{th} inverter is obtained as

$$Q_i = \frac{3}{2}(V_{q,i}I_{d,i} - V_{d,i}I_{q,i}) \tag{27}$$

These power signals are supplied to the inverse droop controller. The inverse droop controller generates the voltage magnitude reference V_i^* and angular frequency reference ω_i^* according to the locally estimated active and reactive powers.

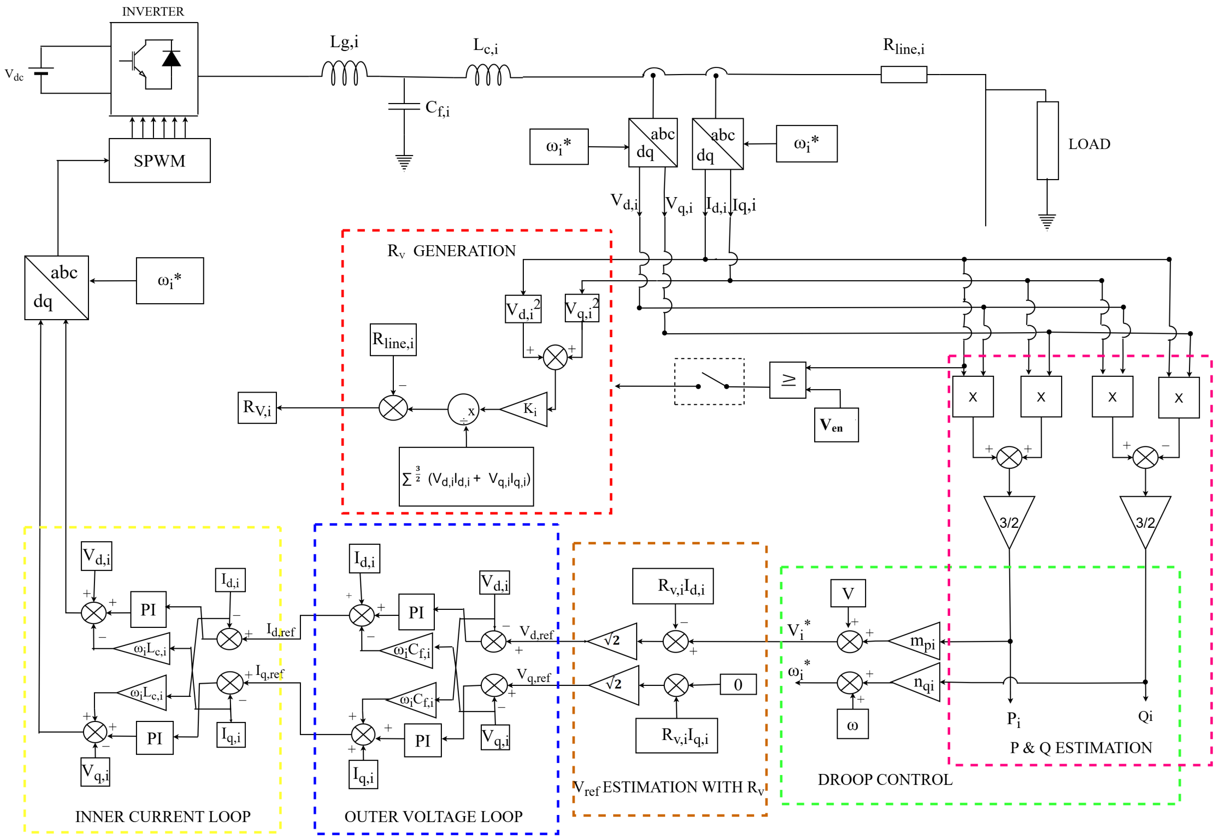

Figure 3. Proposed load adaptive virtual resistance droop control for a single unit.

The droop coefficients are selected according to the rated power capacity of each inverter. For the ith inverter, the reactive-power–frequency droop coefficient and active-power–voltage droop coefficient are designed as

$$n_{q,i} = \frac{\Delta\omega_{\max}}{Q_{rated,i}} \tag{28}$$

$$m_{p,i} = \frac{\Delta V_{\max}}{P_{rated,i}} \tag{29}$$

where $P_{rated,i}$ and $Q_{rated,i}$ are the rated active and reactive powers of the ith inverter, respectively. The terms $\Delta\omega_{\max}$ and $\Delta V_{\max}$ denote the maximum allowable angular-frequency and voltage deviations used for droop design. This rating-based selection allows each inverter to contribute power according to its capacity.

The adaptive virtual resistance mechanism operates by using the locally measured dq voltages and currents. Both the voltage related term and the instantaneous power required in (21) are evaluated from these measurements, and their ratio is processed through the gain K_i, with the feeder resistance $R_{line,i}$ incorporated to represent the actual line characteristics. This computation yields the adaptive virtual resistance $R_{v,i}$ whose value decreases under heavier loading and therefore mitigates the excessive voltage drop associated with a fixed virtual resistance setting. The resulting adaptive resistance is multiplied with the measured current components to obtain the estimated resistive drops in the synchronous frame, and these drops are used to correct the initial voltage references. In this way, the commanded voltage naturally limits the load induced sag ensuring that the terminal magnitude remains within the prescribed regulation limit using only local measurements. The proposed adaptation introduces limited additional computational burden, since the dq-axis voltage and current quantities and the corresponding active-power signal are already available within the inverse-droop control structure. The online evaluation of R_v involves only scalar algebraic operations and does not require iterative optimization or inter-unit communication.

Since the adaptive expression contains voltage and power terms, direct activation during startup may lead to an excessively large or noisy resistance command. Therefore, an activation condition is introduced so that the adaptive branch operates only after the inverter voltage reaches the normal operating region. In the implemented controller, the adaptive branch is enabled when

$$V_{d,i} \geq V_{en} \tag{30}$$

where the enabling threshold is defined as

$$V_{en} = \gamma V_{\text{ph,nom}}. \tag{31}$$

In this study, $\gamma = 0.78$, giving $V_{en} = 180$ V for the considered 400 V line-to-line RMS system. This threshold avoids unrealistic resistance calculation during startup and low-voltage transients. Once the voltage exceeds this threshold, the adaptive virtual resistance is updated according to the load condition and the selected voltage-regulation coefficient.

The applied adaptive resistance is multiplied with the measured current components to obtain the resistive voltage drops in the synchronous frame. These drops are used to modify the droop-generated voltage references according to (25) and (26) before being supplied to the outer voltage loop.

The cascaded voltage and current control loops are used to regulate the inverter terminal voltage and generate the switching commands. The outer voltage loop regulates the inverter terminal voltages by tracking the updated d- and q-axis voltage references. The measured capacitor voltages $V_{d,i}$ and $V_{q,i}$ are compared with $V_{d,ref,i}$ and $V_{q,ref,i}$, respectively, and the resulting voltage errors are processed by PI controllers. The synchronous-frame cross-coupling components $\omega_i C_{f,i} V_{q,i}$ and $\omega_i C_{f,i} V_{d,i}$ are incorporated, as shown in Figure 3, to compensate the capacitor dynamics and preserve decoupled voltage regulation. The outputs of the voltage PI controllers provide the reference currents $I_{d,ref,i}$ and $I_{q,ref,i}$, which serve as the commanded inputs for the inner current loop.

The inner current loop ensures fast and accurate tracking of these reference currents. The measured inductor currents $I_{d,i}$ and $I_{q,i}$ are compared with $I_{d,ref,i}$ and $I_{q,ref,i}$, respectively, and the corresponding current errors are regulated by PI controllers. The synchronous-frame cross-coupling components $\omega_i L_{c,i} I_{q,i}$ and $\omega_i L_{c,i} I_{d,i}$ are included to compensate the dynamic interaction between the d and q axes. The outputs of the current PI controllers generate the modulating voltage commands, which are transformed back to the stationary frame and supplied to the SPWM stage to produce the inverter switching signals.

The PI gains of the cascaded controller are selected using a bandwidth-based design. Since the inner current loop must provide a faster dynamic response, its bandwidth is first selected with respect to the switching frequency as

$$\omega_{0c} = \frac{2\pi f_{sw}}{10} \tag{32}$$

where f_{sw} is the switching frequency and ω_{0c} is the current-loop bandwidth. The current-loop proportional and integral gains are then calculated as

$$K_{p,c} = 2\rho\omega_{0c} L_c - R_c \tag{33}$$

$$K_{i,c} = \omega_{0c}^2 L_c \tag{34}$$

where L_c and R_c are the converter-side filter inductance and resistance, respectively, and ρ is the damping factor.

To maintain proper separation between the cascaded loops, the outer voltage loop is designed to be slower than the inner current loop. Therefore, the voltage-loop bandwidth is selected one decade lower than the current-loop bandwidth as

$$\omega_{0v} = \frac{\omega_{0c}}{10} \tag{35}$$

where ω_{0v} is the voltage-loop bandwidth. Based on this bandwidth, the voltage-loop proportional and integral gains are obtained as

$$K_{p,v} = 2\rho\omega_{0v} C_f \tag{36}$$

$$K_{i,v} = \omega_{0v}^2 C_f \tag{37}$$

where C_f is the filter capacitance. This bandwidth separation allows the inner current loop to respond rapidly to current-reference changes, while the outer voltage loop provides stable reference-current generation and maintains decoupled voltage regulation.

Overall, the proposed control structure enables the adaptive virtual resistance to operate as a primary-layer impedance adjustment mechanism within the inverter controller. The adaptive resistance modifies the voltage reference according to the load condition, feeder resistance, inverter rating, and selected voltage regulation coefficient, while the cascaded voltage and current loops ensure fast dynamic regulation. Therefore, the proposed method improves voltage regulation and proportional power sharing in a fully decentralized manner without requiring communication among inverter units.

3. Verification of the Proposed Control

Table 2 summarizes the electrical characteristics, feeder impedances and filter components adopted in the simulation model. These parameters provide a consistent framework for evaluating the effect of the proposed adaptive strategy on voltage regulation and power sharing accuracy under varying load conditions.

Table 2. System parameters of the two-inverter microgrid.

Parameters	DG1	DG2
DC-link voltage (V_{dc})	800 V	800 V
Line-to-line rms voltage (V_{LL})	400 V	400 V
Nominal frequency (f)	50 Hz	50 Hz
Rated active power (P_{rated})	12 kW	8 kW
Rated reactive power (Q_{rated})	5 kVAr	4 kVAr
Converter side inductance (L_c)	0.5 mH	0.5 mH
Converter side resistance (R_c)	0.3 mΩ	0.3 mΩ
Grid side inductance (L_g)	0.3 mH	0.3 mH
Grid side resistance (R_g)	0.2 mΩ	0.2 mΩ
Filter capacitance (C_f)	30.1 µF	30.1 µF
Feeder Resistance (R_{line})	0.005 Ω	0.02 Ω
Switching frequency (f_{sw})	15 kHz	15 kHz
Voltage regulation coefficient (ϵ)	0.02	0.02
Baseline fixed R_v	0.62 Ω	0.901 Ω
Damping factor (ρ)	1.1	1.1

A detailed model of the two inverter microgrid is developed to evaluate the performance of the proposed load adaptive virtual resistance based droop control. The test system consists of two voltage source inverters (VSI) of different rated capacities operating in parallel on a common AC bus. Each inverter is interfaced through an LCL filter and its own feeder resistance, resulting in unavoidable line impedance mismatch between the units. The droop coefficients of each unit are chosen accordingly, to maintain proportional power sharing according to the inverter ratings. The adaptive virtual resistance block is enabled in both inverters, and its value is continuously updated using the locally measured dq frame voltages and currents.

To verify the improvement over the conventional fixed R_v design, the baseline virtual resistance is set to 0.62 Ω for DG1 and 0.901 Ω for DG2. In the proposed method, R_v is adjusted adaptively according to the operating condition. A base load of 9 kW active power and 2 kVAr reactive power is initially applied. At $t = 0.3$ s, an additional load of 4 kW and 2 kVAr is introduced, and at $t = 0.6$ s it is removed to assess the transient behavior of the system.

Figure 4 compares the RMS terminal voltages of conventional fixed R_v droop control with load adaptive R_v droop control under this loading condition. The RMS values are computed from the phase voltages using the continuous RMS block in Simulink, with all circuit and control parameters identical to those listed in Table 2 for both cases. With the fixed R_v, the PCC voltages of the two inverters drop to 221 V, which is clearly outside the 2$\%$ limit, Whereas under the proposed load adaptive strategy the terminal voltages settle around 230 V for both units, remaining within the prescribed regulation limit.This comparison confirms that the adaptive R_v method effectively compensates the feeder impedance mismatch and enables the PCC voltage settle very close to the nominal value even when the inverters have unequal power ratings.

Furthermore, the active and reactive power responses during the disturbance are shown in Figure 5 for DG1 and DG2. Figure 5a,c represent the conventional fixed R_v droop method for a load step at 0.3 s and its removal at 0.6 s. For a nominal 9 kW load, DG1 and DG2 supply approximately 5100 W and 3350 W, respectively, while during the nominal 13 kW interval they deliver around 7300 W and 5050 W. Although the active power is shared approximately according to the inverter rating proportions, the combined active power remains lower than the nominal load demand because of the reduced PCC voltage under the fixed R_v condition. The reactive power response exhibits a more noticeable deviation from the desired proportional sharing. At the lower load level, DG1 and DG2 supply roughly 1000 var each, while at the higher load level they deliver about 2300 var and 1850 var, respectively. Overall, the fixed-R_v case maintains approximately proportional active-power sharing, while the reactive-power sharing shows a more noticeable deviation from the desired proportion between the two DG units.

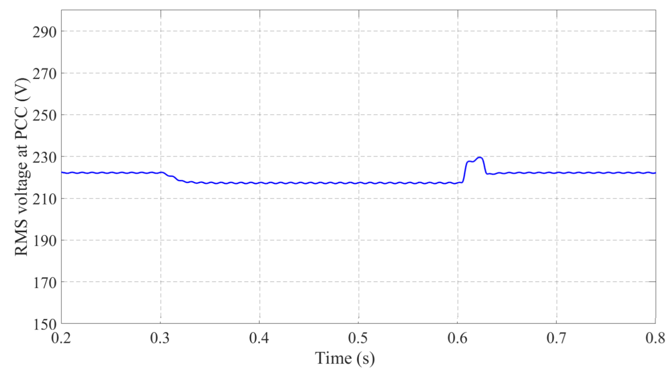

(a)

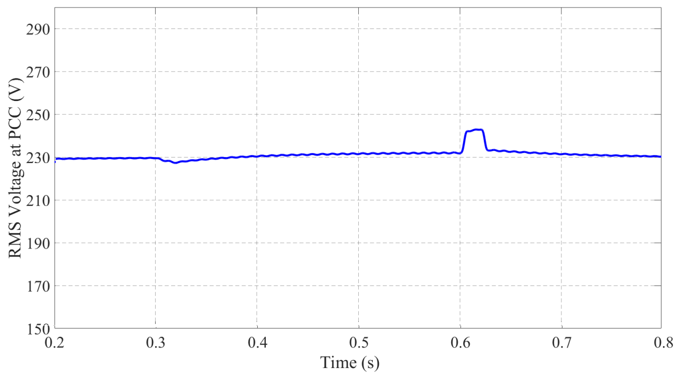

(b)

Figure 4. RMS voltage response at the PCC during load step changes at 0.3 s and 0.6 s: (**a**) conventional fixed virtual resistance method; (**b**) proposed load-adaptive virtual resistance method.

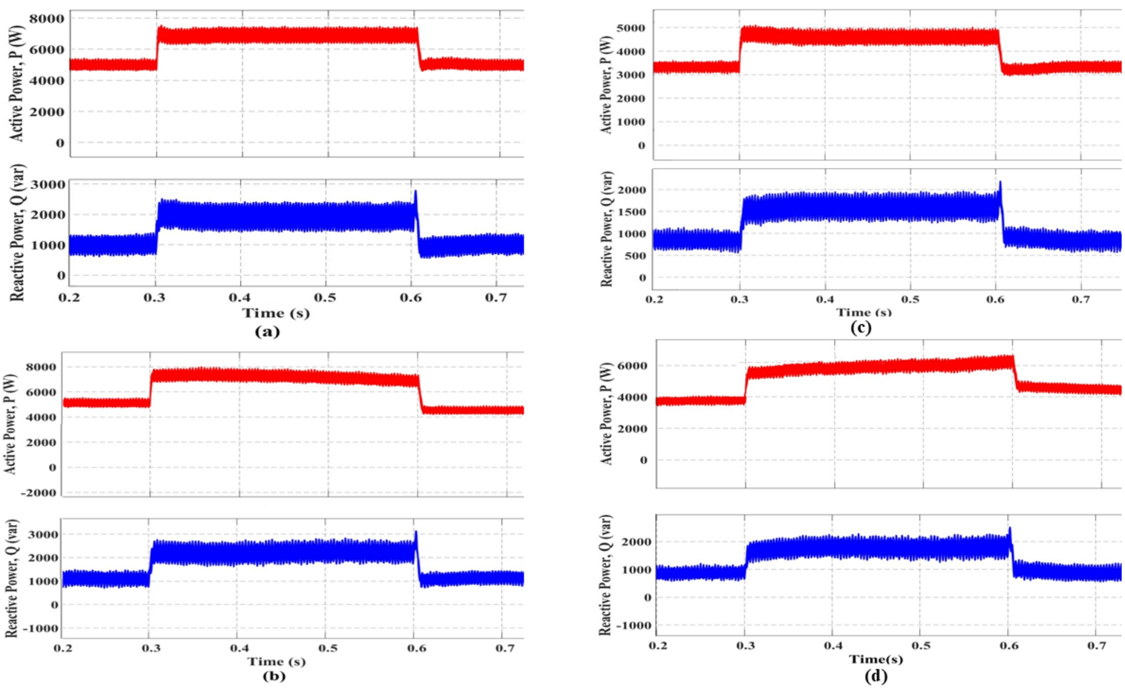

Figure 5. Dynamic active and reactive power responses of DG1 and DG2 during load step changes at 0.3 s and 0.6 s: (**a**) DG1 with conventional fixed virtual resistance; (**b**) DG1 with the proposed load-adaptive virtual resistance; (**c**) DG2 with conventional fixed virtual resistance; and (**d**) DG2 with the proposed load-adaptive virtual resistance.

In contrast, Figure 5b,d depict the transient active and reactive power responses of the proposed control scheme. Before the load change, DG1 delivers 5332 W and DG2 supplies 3668 W, which is nearly equal to their proportional share of the 9 kW load. When the load increases at 0.3 s, the total power settles around 13 kW, with DG1 providing approximately 7701 W and DG2 supplying 5300 W, again closely matching their proportional load contributions. The reactive power sharing is very close to the expected proportional behavior, with DG1 supplying about 1184 VAR and 2370 VAR for total reactive loads of 2000 VAR and 4000 VAR, while DG2 delivers 816 VAR and 1630 VAR. Overall, the reactive power sharing exhibits excellent proportional accuracy across all operating points, further validating the effectiveness of the proposed control scheme. These results confirm that the proposed method maintains the PCC voltage close to its nominal value while enabling the intended active and reactive power demand to be supplied with accurate proportional sharing between the inverter units.

Figure 6 presents the current sharing between DG1 and DG2 for the proposed system during the transient loading event. When the additional load is applied at 0.3 s, the total power demand increases, and both inverters respond by proportionally raising their output currents to supply the additional load. This coordinated increase demonstrates effective load sharing under the proposed control scheme. Once the load is removed at 0.6 s, the currents in both DG units decrease and return smoothly to their initial values.

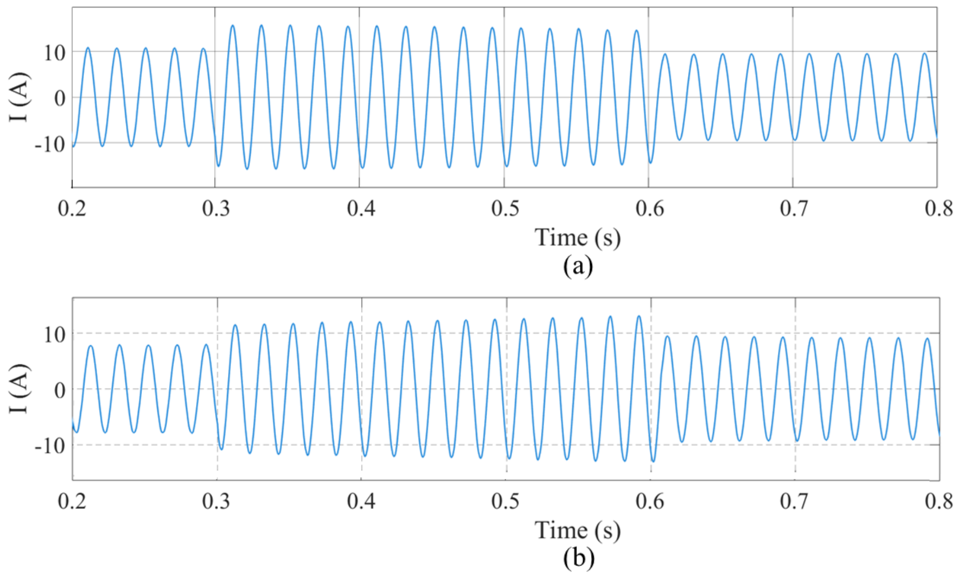

Figure 6. Current sharing behavior of DG1 and DG2 for a representative phase under the proposed adaptive control scheme during dynamic loading: (**a**) DG1 current; (**b**) DG2 current.

Figure 7 shows the corresponding PCC voltage for a single phase, which remains essentially unchanged throughout the loading and unloading intervals, confirming that the terminal voltage is consistently maintained despite the variations in current demand.

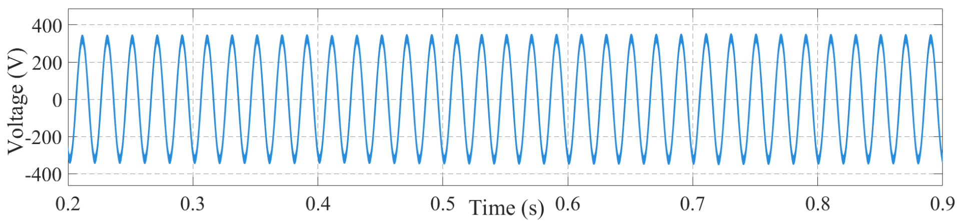

Figure 7. PCC voltage of a representative phase under the proposed adaptive control during the load disturbance.

Figure 8 shows the frequency responses of DG1 and DG2 under the proposed load-adaptive virtual resistance control during the dynamic load variation. The frequencies of both inverter units remain closely matched throughout the operating interval, indicating synchronized operation of the parallel DGs. Following the load increase at $t = 0.3$ s, the frequency rises according to the inverse-droop characteristic. The maximum frequencies of DG1 and DG2 are 50.1241 Hz and 50.1247 Hz, respectively, corresponding to a maximum deviation of approximately 0.125 Hz (0.25%) from the nominal 50 Hz. After the additional load is removed at $t = 0.6$ s, the frequencies decrease toward their pre-disturbance operating values. These results demonstrate that the proposed control maintains coordinated frequency behaviour during the considered load changes.

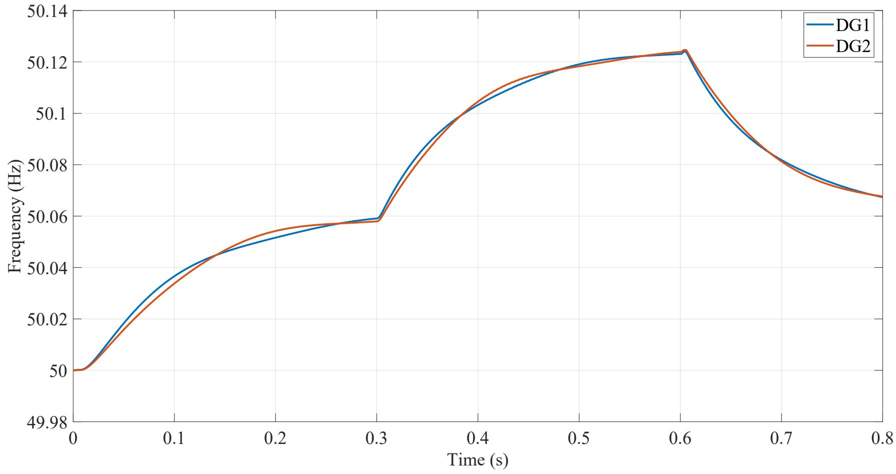

Figure 8. Frequency responses of DG1 and DG2 under the proposed load-adaptive virtual resistance control during dynamic load variation.

Figure 9 illustrates the PCC voltage behaviour under varying load (9–17 kW) for both the proposed adaptive controller and the conventional fixed R_v method. The proposed controller maintains the PCC voltage very close to the nominal value (230.94 V) across the entire loading range, with only a small and smooth variation between 229 V and 231 V. The voltage profile remains nearly flat, demonstrating that the adaptive mechanism continuously counteracts the effect of feeder impedance mismatch and prevents the voltage from drooping as the load increases. This behaviour confirms that the proposed method achieves strong voltage regulation, ensuring that the PCC voltage stays tightly regulated around the desired nominal level even at higher loading conditions. In contrast, the conventional fixed R_v scheme exhibits a progressive and noticeable voltage drop with increasing load, where the PCC voltage declines from approximately 222 V at 9 kW to 216.8 V at 17 kW. This downward slope indicates that the conventional fixed R_v controller is unable to compensate for changing loading conditions, resulting in poor voltage support and significant deviation from the nominal value. Overall, the comparison clearly highlights the superior voltage regulation capability of the proposed adaptive method, as it preserves the PCC voltage near its nominal target across the entire operating range, whereas the conventional approach suffers from steady voltage degradation as the load increases.

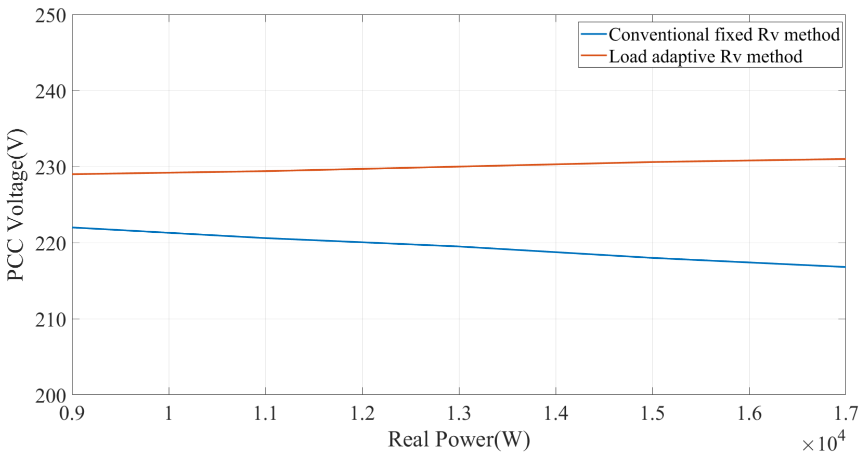

Figure 9. PCC voltage variation with real power loading for the conventional fixed virtual resistance method and the proposed load-adaptive virtual resistance method.

The harmonic performance of the system is evaluated through FFT analysis of the PCC voltage, and the corresponding THD values are shown in Figure 10. Under the rated operating condition, the inverter exhibits a voltage THD of 4%, indicating low harmonic distortion under the considered operating condition. This confirms that the proposed control strategy maintains good voltage quality during islanded operation.

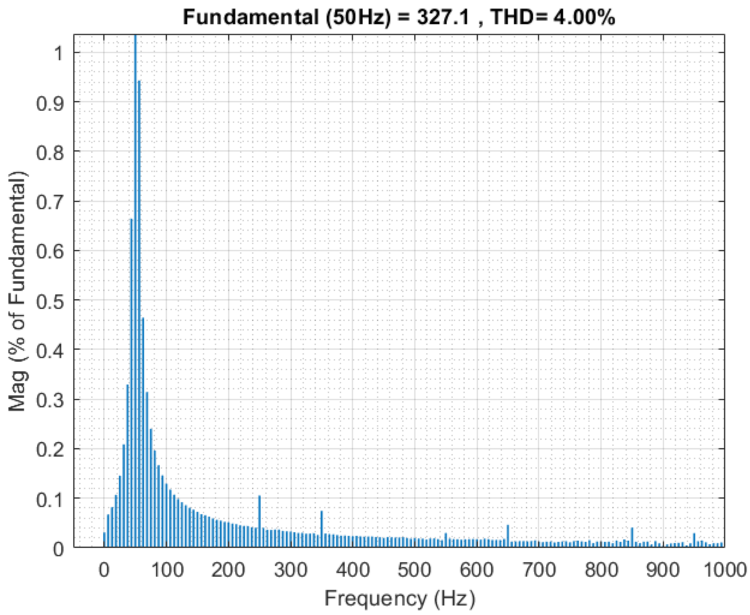

Figure 10. THD analysis of the PCC voltage.

3.1. Quantitative Performance Comparison

The quantitative performance of the conventional fixed virtual resistance method and the proposed load adaptive virtual resistance method is summarized in Tables 3 and 4. Table 3 evaluates the active and reactive power-sharing accuracy with respect to the ideal rating-based sharing ratio between DG1 and DG2, while Table 4 compares the PCC voltage range, maximum voltage deviation, and voltage THD. Overall, the quantitative results confirm that the proposed adaptive virtual resistance method achieves improved voltage regulation and more accurate rating-based power sharing while maintaining acceptable harmonic performance.

Table 3. Comparison of rating-based active and reactive power sharing performance.

Performance Metric	**Ideal Rating-Based Sharing**	**Conventional Fixed R_v**	**Proposed Adaptive R_v**
Active power sharing (DG1:DG2)	59.24%:40.76%	59.74%:40.26%	59.24%:40.76%
Reactive power sharing (DG1:DG2)	59.24%:40.76%	52.71%:47.29%	59.23%:40.77%

Table 4. Quantitative comparison of voltage regulation and harmonic performance.

Performance Metric	**Conventional Fixed R_v**	**Proposed Adaptive R_v**
PCC voltage range	216.8–222 V	229–231 V
Maximum voltage deviation	6.12%	0.84%
PCC voltage THD	4.6%	4.0%

4. Conclusions

This paper presented a novel load-adaptive virtual-resistance-based droop control strategy for the decentralized operation of low-voltage islanded microgrids with impedance mismatch. The proposed approach is specifically designed to address the challenges associated with resistive feeder characteristics and unequal line impedances commonly encountered in low-voltage microgrids. This control strategy effectively compensates for the trade-off between voltage regulation and accurate power sharing by dynamically adjusting the virtual resistance in response to load changes. In contrast to the conventional fixed virtual resistance scheme, which exhibits significant voltage sag under increased loading conditions, the adaptive strategy effectively compensates for feeder impedance mismatch and prevents excessive voltage drop during heavy loading. Furthermore, the proposed control scheme achieves accurate active and reactive power sharing based on the respective inverter ratings without relying on any communication links.This fully decentralized implementation enhances system reliability and achieves satisfactory voltage and frequency regulation under the considered operating conditions without requiring a secondary control layer. The simulation results demonstrate that the proposed method maintains voltage regulation well within the

https://doi.org/10.53941/perat.2026.100008

prescribed limit over a wide range of load variations, including dynamic load changes, while simultaneously ensuring accurate power sharing. Overall, the proposed load-adaptive virtual resistance–based droop control provides a simple, fully decentralized, and effective solution for improving voltage regulation and power-sharing performance in low-voltage islanded microgrids.

5. Biographies of the Authors

Ashitha Pallen is currently working toward the Ph.D. degree at Federation University Australia. Her research interests include power converters, microgrids and advanced control of grid-forming inverters.

Jiefeng Hu received a Ph.D. in electrical engineering from the University of Technology Sydney, Australia. He is currently a Professor and Stream Leader of the Centre for New Energy Transition Research at Federation University Australia. His expertise is in grid integration of renewable energy.

Syed Islam received the Ph.D. degree from King Fahd University of Petroleum and Minerals, Saudi Arabia, in 1988. He is currently an Emeritus Distinguished Professor at Federation University Australia. His expertise is in power systems.

Author Contributions

A.P.: conceptualization, methodology, software, validation, investigation, visualization, writing—original draft preparation; J.H.: conceptualization, methodology, supervision, writing—review and editing; S.I.: supervision, writing—review and editing. All authors have read and agreed to the published version of the manuscript.

Funding

This research received no external funding.

Institutional Review Board Statement

Not applicable.

Informed Consent Statement

Not applicable.

Data Availability Statement

The data supporting the findings of this study are available from the corresponding author upon reasonable request.

Conflicts of Interest

The authors declare no conflict of interest.

Use of AI and AI-Assisted Technologies

During the preparation of this work, the authors used ChatGPT (OpenAI) for language refinement.

References

1. Hu, J.; Shan, Y.; Cheng, K.W.; et al. Overview of Power Converter Control in Microgrids—Challenges, Advances, and Future Trends. *IEEE Trans. Power Electron.* **2022**, *37*, 9907–9922. https://doi.org/10.1109/tpel.2022.3159828.
2. Sepehrzad, R.; Mahmoodi, A.; Ghalebi, S.Y.; et al. Intelligent hierarchical energy and power management to control the voltage and frequency of micro-grids based on power uncertainties and communication latency. *Electr. Power Syst. Res.* **2022**, *202*, 107567. https://doi.org/10.1016/j.epsr.2021.107567.

3. Nair, R.P.; Kanakasabapathy, P. Design and implementation of decoupled controller for interlinking converter in hybrid microgrid. *Electr. Power Syst. Res.* **2025**, *248*, 111852. https://doi.org/10.1016/j.epsr.2025.111852.
4. Guerrero, J.M.; Chandorkar, M.; Lee, T.L.; et al. Advanced Control Architectures for Intelligent Microgrids—Part I: Decentralized and Hierarchical Control. *IEEE Trans. Ind. Electron.* **2013**, *60*, 1254–1262. https://doi.org/10.1109/tie.2012.2194969.
5. Abouassy, A.M.; Alafnan, H.; Mansour, D.E.A.; et al. An Improved Droop-Based Adaptive Virtual Impedance for Accurate Power Sharing Among Multiple DGs in Islanded Microgrid. *IEEE Access* **2025**, *13*, 108918–108933. https://doi.org/10.1109/access.2025.3581481.
6. Keyvani-Boroujeni, B.; Fani, B.; Shahgholian, G.; et al. Virtual Impedance-Based Droop Control Scheme to Avoid Power Quality and Stability Problems in VSI-Dominated Microgrids. *IEEE Access* **2021**, *9*, 144999–145011. https://doi.org/10.1109/access.2021.3122800.
7. Zhang, L.; Zheng, H.; Hu, Q.; et al. An Adaptive Droop Control Strategy for Islanded Microgrid Based on Improved Particle Swarm Optimization. *IEEE Access* **2020**, *8*, 3579–3593. https://doi.org/10.1109/access.2019.2960871.
8. Zhong, Q.C.; Zeng, Y. Universal Droop Control of Inverters with Different Types of Output Impedance. *IEEE Access* **2016**, *4*, 702–712. https://doi.org/10.1109/access.2016.2526616.
9. Zhong, Q.C.; Ming, W.L.; Zeng, Y. Self-Synchronized Universal Droop Controller. *IEEE Access* **2016**, *4*, 7145–7153. https://doi.org/10.1109/access.2016.2616115.
10. Tao, X.; Zhang, L.; Wang, F. Droop Control Optimization Strategy for Parallel Inverters in a Microgrid Based on an Improved Population Division Fruit Fly Algorithm. *IEEE Access* **2022**, *10*, 24877–24894. https://doi.org/10.1109/access.2022.3145965.
11. Zhang, L.; Sun, L.; Xu, W.; et al. Voltage droop control optimization in microgrid integration with VSC HVDC systems and wind power plants for enhanced dynamic stability. *Electr. Power Syst. Res.* **2026**, *252*, 112363. https://doi.org/10.1016/j.epsr.2025.112363.
12. He, J.; Li, Y.W. Analysis, Design, and Implementation of Virtual Impedance for Power Electronics Interfaced Distributed Generation. *IEEE Trans. Ind. Appl.* **2011**, *47*, 2525–2538. https://doi.org/10.1109/tia.2011.2168592.
13. Yu, X.; Khambadkone, A.M.; Wang, H.; et al. Control of Parallel-Connected Power Converters for Low-Voltage Microgrid—Part I: A Hybrid Control Architecture. *IEEE Trans. Power Electron.* **2010**, *25*, 2962–2970. https://doi.org/10.1109/tpel.2010.2087393.
14. Chen, J.; Yue, D.; Dou, C.X.; et al. A Virtual Complex Impedance based P-V Droop Method for Parallel-connected Inverters in Low-voltage AC Microgrids. *IEEE Trans. Ind. Inform.* **2021**, *17*, 1763–1773. https://doi.org/10.1109/tii.2020.2997054.
15. Shu, L.; Chen, W.; Jiang, X. Decentralized Control for Fully Modular Input-Series Output-Parallel (ISOP) Inverter System Based on the Active Power Inverse-Droop Method. *IEEE Trans. Power Electron.* **2018**, *33*, 7521–7530. https://doi.org/10.1109/tpel.2017.2773559.
16. Wang, X.; Li, Y.W.; Blaabjerg, F.; et al. Virtual-Impedance-Based Control for Voltage-Source and Current-Source Converters. *IEEE Trans. Power Electron.* **2015**, *30*, 7019–7037. https://doi.org/10.1109/tpel.2014.2382565.
17. Guan, Y.; Guerrero, J.M.; Zhao, X.; et al. A New Way of Controlling Parallel-Connected Inverters by Using Synchronous-Reference-Frame Virtual Impedance Loop—Part I: Control Principle. *IEEE Trans. Power Electron.* **2016**, *31*, 4576–4593. https://doi.org/10.1109/tpel.2015.2472279.
18. Vasquez, J.C.; Guerrero, J.M.; Savaghebi, M.; et al. Modeling, Analysis, and Design of Stationary-Reference-Frame Droop-Controlled Parallel Three-Phase Voltage Source Inverters. *IEEE Trans. Ind. Electron.* **2013**, *60*, 1271–1280. https://doi.org/10.1109/tie.2012.2194951.
19. Qi, Y.; Tang, Y.; Potti, K.R.R.; et al. Robust Power Sharing Control for Parallel Three-phase Inverters Against Voltage Measurement Errors. *IEEE Trans. Power Electron.* **2020**, *35*, 13590–13601. https://doi.org/10.1109/tpel.2020.2993290.
20. Pournazarian, B.; Seyedalipour, S.S.; Lehtonen, M.; et al. Virtual Impedances Optimization to Enhance Microgrid Small-Signal Stability and Reactive Power Sharing. *IEEE Access* **2020**, *8*, 139691–139705. https://doi.org/10.1109/access.2020.3013031.
21. Wei, B.; Marzabal, A.; Ruiz, R.; et al. DAVIC: A New Distributed Adaptive Virtual Impedance Control for Parallel-Connected Voltage Source Inverters in Modular UPS System. *IEEE Trans. Power Electron.* **2019**, *34*, 5953–5968. https://doi.org/10.1109/tpel.2018.2869870.
22. Macana, C.A.; Pota, H.R. Adaptive synchronous reference frame virtual impedance controller for accurate power sharing in islanded ac-microgrids: A faster alternative to the conventional droop control. In Proceedings of the 2017 IEEE Energy Conversion Congress and Exposition (ECCE), Cincinnati, OH, USA, 1–5 October 2017; pp. 3728–3735. https://doi.org/10.1109/ecce.2017.8096659.
23. Mahmood, H.; Michaelson, D.; Jiang, J. Accurate Reactive Power Sharing in an Islanded Microgrid Using Adaptive Virtual Impedances. *IEEE Trans. Power Electron.* **2015**, *30*, 1605–1617. https://doi.org/10.1109/tpel.2014.2314721.
24. An, R.; Liu, Z.; Liu, J. Successive-Approximation-Based Virtual Impedance Tuning Method for Accurate Reactive Power Sharing in Islanded Microgrids. *IEEE Trans. Power Electron.* **2021**, *36*, 87–102. https://doi.org/10.1109/tpel.2020.3001037.
25. Vijay, A.S.; Parth, N.; Doolla, S.; et al. An Adaptive Virtual Impedance Control for Improving Power Sharing Among Inverters in Islanded AC Microgrids. *IEEE Trans. Smart Grid* **2021**, *12*, 2991–3003. https://doi.org/10.1109/tsg.2021.3062391.
26. Fan, B.; Li, Q.; Wang, W.; et al. A Novel Droop Control Strategy of Reactive Power Sharing Based on Adaptive Virtual Impedance in Microgrids. *IEEE Trans. Ind. Electron.* **2022**, *69*, 11335–11347. https://doi.org/10.1109/tie.2021.3123660.

27. Dheer, D.K.; Gupta, Y.; Doolla, S. A Self-Adjusting Droop Control Strategy to Improve Reactive Power Sharing in Islanded Microgrid. *IEEE Trans. Sustain. Energy* **2020**, *11*, 1624–1635. https://doi.org/10.1109/tste.2019.2933144.
28. Prakash, S.; Nougain, V.; Mishra, S. Adaptive Droop-Based Control for Active Power Sharing in Autonomous Microgrid for Improved Transient Performance. *IEEE J. Emerg. Sel. Top. Power Electron.* **2021**, *9*, 3010–3018. https://doi.org/10.1109/jestpe.2020.2988712.
29. Hoang, T.V.; Lee, H.H. Accurate Power Sharing with Harmonic Power for Islanded Multibus Microgrids. *IEEE J. Emerg. Sel. Top. Power Electron.* **2019**, *7*, 1286–1299. https://doi.org/10.1109/jestpe.2018.2865207.
30. Qian, H.; Xu, Q.; Du, P.; et al. Distributed Control Scheme for Accurate Power Sharing and Fixed Frequency Operation in Islanded Microgrids. *IEEE Trans. Ind. Electron.* **2021**, *68*, 12229–12238. https://doi.org/10.1109/tie.2020.3047014.
31. Qi, Y.; Lin, P.; Wang, Y.; et al. Two-Dimensional Impedance-Shaping Control with Enhanced Harmonic Power Sharing for Inverter-Based Microgrids. *IEEE Trans. Power Electron.* **2019**, *34*, 11407–11418. https://doi.org/10.1109/tpel.2019.2898670.
32. Lu, J.; Zhao, M.; Golestan, S.; et al. Distributed Event-Triggered Control for Reactive, Unbalanced, and Harmonic Power Sharing in Islanded AC Microgrids. *IEEE Trans. Ind. Electron.* **2022**, *69*, 1548–1560. https://doi.org/10.1109/tie.2021.3057018.
33. Naresh Kumar, V.; Parida, S.K. Parameter Optimization of Universal Droop and Internal Model Controller for Multi Inverter-Fed DGs Based on Accurate Small-Signal Model. *IEEE Access* **2019**, *7*, 101928–101940. https://doi.org/10.1109/access.2019.2931151.